Lab on a Chip

Real-time Imaging of Nanobubble Ultrasound Contrast Agent Flow, Extravasation, and Diffusion through an Extracellular Matrix using a Microfluidic Model

Journal:	*Lab on a Chip*
Manuscript ID	LC-ART-06-2023-000514
Article Type:	Paper
Date Submitted by the Author:	13-Jun-2023
Complete List of Authors:	Cooley, Michaela; Case Western Reserve University, Department of Biomedical Engineering Wulftange, William; Case Western Reserve University, Biomedical Engineering Wegierak, Dana; Case Western Reserve University, Biomedical Engineering Goreke, Utku; Case Western Reserve University, Department of Mechanical and Aerospace Engineering Abenojar, Eric; Case Western Reserve University, Radiology Gurkan, Umut; Case Western Reserve University, Mechanical and Aerospace Engineering Exner, Agata; Case Western Reserve University, Dept. of Radiology

Real-time Imaging of Nanobubble Ultrasound Contrast Agent Flow, Extravasation, and Diffusion through an Extracellular Matrix using a Microfluidic Model

Michaela B. Cooley[1a], William J. Wulftange[1a], Dana Wegierak[1], Utku Goreke[2], Eric C. Abenojar[3], Umut A. Gurkan[1,2b], Agata A. Exner[1,3b]

[1]Department of Biomedical Engineering, Case Western Reserve University, Cleveland, Ohio 44106, United States

[2]Department of Mechanical and Aerospace Engineering, Case Western Reserve University, Cleveland, Ohio 44106, United States

[3]Department of Radiology, Case Western Reserve University, Cleveland, Ohio 44106, United States

[a]Michaela B. Cooley and William J. Wulftange are co-first authors

[b]Umut A. Gurkan and Agata A. Exner are co-corresponding authors

*To whom correspondence should be addressed:
Dr. Agata A. Exner
Department of Radiology
Case Western Reserve University School of Medicine
Cleveland, OH, 44106
agata.exner@case.edu
216-368-6727

Dr. Umut Gurkan
Department of Mechanical Engineering
Case Western Reserve University
Cleveland, OH, 44106
umut@case.edu
216-368-6447

Abstract

Lipid shell-stabilized nanoparticles with a perfluorocarbon gas-core, or nanobubbles, have recently attracted attention as a new contrast agent for molecular ultrasound imaging and image-guided therapy. Due to their small size (~275 nm diameter) and flexible shell, nanobubbles have been shown to extravasate through hyperpermeable vasculature (e.g., in tumors). However, little is known about the dynamics and depth of extravasation of intact, acoustically active nanobubbles. Accordingly, in this work, we developed a microfluidic chip with a lumen and extracellular matrix (ECM) and imaging method that allows real-time imaging and characterization of the extravasation process with high-frequency ultrasound. The microfluidic device has a lumen and is surrounded by an extracellular matrix with tunable porosity. The combination of ultrasound imaging and the microfluidic chip advantageously produces real-time images of the entire length and depth of the matrix. This captures the matrix heterogeneity, offering advantages over other imaging techniques with smaller fields of view. Results from this study show that nanobubbles diffuse through a 1.3 μm pore size (2 mg/mL) collagen I matrix 25x faster with a penetration depth that was 0.19 mm deeper than a 3.7 μm (4 mg/mL) matrix. In the 3.7 μm pore size matrix, nanobubbles diffused 92x faster than large nanobubbles (~875 nm diameter). Decorrelation time analysis was successfully used to differentiate flowing and extra-luminally diffusing nanobubbles. In this work, we show for the first time that combination of an ultrasound-capable microfluidic chip and real-time imaging provided valuable insight into spatiotemporal nanoparticle movement through a heterogeneous extracellular matrix. This work could help accurately predict parameters (e.g., injection dosage) that improve translation of nanoparticles from *in vitro* to *in vivo* environments.

Keywords: Microfluidics, ultrasound imaging, nanobubble ultrasound contrast agents, extravasation, extracellular matrix, cancer

Introduction

Nanoparticles are an attractive delivery system for conditions involving hyperpermeable vasculature (e.g., oncology, diabetes) because they can escape the intravascular space and penetrate the surrounding tissue. Other benefits of nanoparticle-based therapeutics include protection of fragile cargo, addition of molecular targeting moieties, prolonged *in vivo* circulation time, and reduced systemic toxicity (1–3). Due to these and other benefits, nanoparticles are often leveraged for diseases like cancer. There are currently 114 nanoparticle-based anticancer drugs listed as recruiting or active in clinical trials (ClinicalTrials.gov, U.S. National Library of Medicine). However, translation of nanomedicine into the clinic has been less efficacious than anticipated with only 22 medicines FDA and/or EMA (European Medicines Agency) approved for cancer as of 2019 (4). By some accounts, only 0.7% of administered nanoparticles reach their target and stay there long enough to release their drug (5). This is largely due to the challenges of making sure that nanoparticles both accumulate and are retained at their target site.

The extravasation of nanoparticles is a critical determinant to their success. Yet, the tools available to study this process are limited. Some current *in vivo* methods include intravital microscopy and optical imaging; however, most analyses are still carried out with postmortem histology via fluorescent microscopy methods, which have considerable limitations (6–12). Intravital microscopy is expensive, not widely available, and has an invasive setup. Histological analysis requires that the sample is removed from its native environment and analysis does not occur in real-time. To study the extravasation process *in vitro*, microfluidic systems that mimic native vasculature have been developed (13,14). Most microfluidic platforms are compatible with standard optical imaging techniques, but quantification of real-time extravasation can be a challenge (15–17). For instance, when imaging biological samples in real-time with microscopy, images are produced in the horizontal plane with a small field of view (e.g., 4 mm for a 4x objective lens). The field of view decreases significantly with increasing resolution. Most microscopy methods image in a single plane, but it is possible to capture the 3D architecture of a sample with

confocal microscopy. However, 3D confocal acquisition is not conducted in real-time and can be time intensive. Fluorescent microscopy also requires attaching fluorophores or stains to the imaged structures and particles, which increases preparation time and can alter the surface structure of the sample. All of these methods have limitations that prevent a complete evaluation of nanoparticles from being realized.

Unlike standard microscopy methods, biomedical ultrasound is a modality that is capable of real-time (>20 frames per second) imaging with a large penetration depth (e.g., up to 3.5 cm for a 10 MHz clinical transducer) and a wide field of view (18). Ultrasound imaging has been used previously alongside microfluidics to study chemical reactions and acoustic cavitation, and size biological cells. Microfluidics have also been used previously in the ultrasound contrast agent (UCA) field for production of monodisperse MBs and nanoemulsions (19–29). However, to our knowledge ultrasound has not been used to visualize the extravasation kinetics of nanoparticles into the extracellular matrix in a microfluidics-based model system.

UCAs, nanobubbles (NBs) and microbubbles (MBs), have a high signal-to-noise ratio and can be used to differentiate the location of the bubbles from the background tissue (30). An advantage of NBs is that they are capable of extravasation due to their small size; thus, making them an excellent nanoparticle for studying the extravasation and diffusion process through an extracellular matrix (ECM) (31). Herein, we describe a novel, ultrasound-capable, microfluidic device to study the real-time extravasation of NBs, and other nanoparticles, into and through an ECM. The design of the microfluidic chip allows for the observation of extravasation kinetics in a highly controlled and straightforward system, compared to other *in vitro* and *in vivo* systems. The simplicity and tunability of the system emphasize isolation of specific parameters, such as the effect of particle size, on extravasation capacity. By integrating ultrasound with the chip, we observed extravasation of NBs in real-time through the entire depth of the ECM using both B-mode and non-linear contrast (NLC) mode imaging, offering significant advantages over optical microscopy techniques with existing microfluidic platforms.

Methods and Materials

3D Microfluidic Chip Fabrication

The ECM chamber (**Fig. 1A-D**) geometry was formed via two laser micro-machined 1 mm polymethyl methacrylate (PMMA) layers obtained from McMaster-Carr (Elmhurst, IL). Semi-circles were etched into PMMA layers that, when stacked formed side channels through which a 25G needle (Component Supply Company; Mentor, OH) could be inserted. PMMA layers were adhered together using laser micro-machined 50 μm double-sided adhesive (DSA) from 3M (Saint Paul, MN). The PMMA layers formed the ECM chamber and were sandwiched between two outer DSA layers. For ultrasound compatibility, Sylgard™ 184 polydimethylsiloxane (PDMS) (The Dow Chemical Company; Midland, MI) was cast (9:1 ratio) and cured overnight on a leveling plate to achieve a thickness of approximately 1.5 mm. PDMS sheets were cured at 80 °C for 20 minutes and cut into 56 mm x 22 mm sheets with 0.5 mm diameter inlet and outlet holes and 0.5 mm ECM injection ports. To facilitate covalent bonding between the top DSA and PDMS layers, both were treated with oxygen plasma and firmly pressed together (**Fig. 1B, Supplemental Fig. 1A)**. It was essential to use PDMS for the top and bottom layers instead of PMMA to decrease reflection of ultrasound waves. Further images of the fully assembled device are shown in **Supplemental Fig. 1A**. Following assembly, the devices were incubated at 37 °C overnight to increase bond strength. Blunt tip 1.5” 25G needles were incubated in bovine serum albumin (Sigma-Aldrich; St. Louis, MO) for 30 minutes and then inserted into the side channels of the chip. Rat collagen I (Advanced Biomatrix; Carlsbad, CA) was then mixed according to the manufacturer’s instructions to a final concentration of 4 mg/mL (1.3 μm pores) or 2 mg/mL (3.7 μm pores) and injected into the ECM port at the top of the device. The collagen matrix-loaded devices were then incubated for 1 hour at 37 °C after which point the 25G needles could be removed (32,33). To prevent the introduction of air bubbles into the lumen, PBS was injected while simultaneously removing the blunt-tip needles. Inlet and outlet microbore tubing (Cole-Parmer; Vernon Hills, IL) were then attached and all unused ports were sealed with 5-minute epoxy (ITW Performance Polymers; Danvers, MA).

The epoxy was cured for a minimum of 45 minutes before submersion in water for ultrasound imaging. The composition and layers of the microfluidic chip are depicted in **Fig. 1B** and the region through which ultrasound data was collected is shown in **Fig. 1C**. Cutaways schematics can be seen in **Supplemental Fig. 1A**.

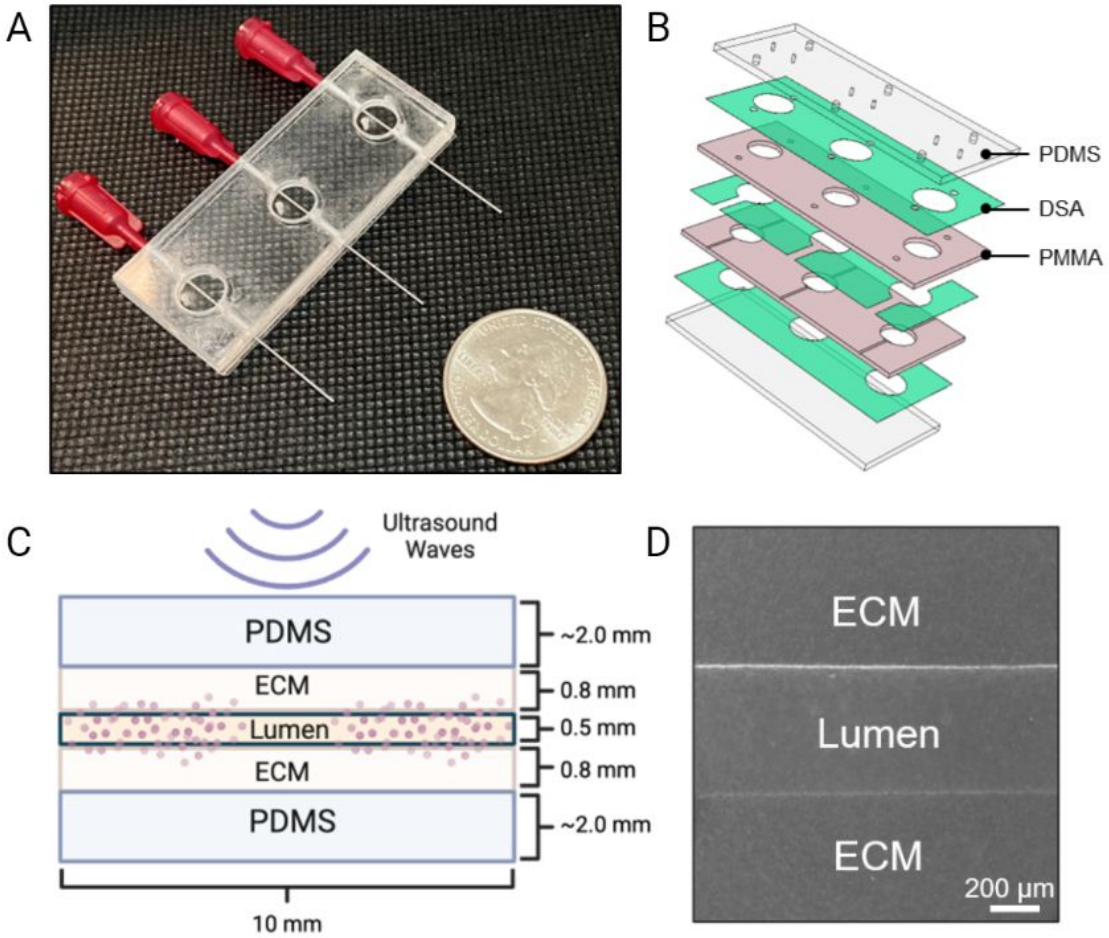

Fig. 1. Microfluidic chip design and fabrication. (A) Photograph of the microfluidic device with a US quarter for scale. (B) Exploded view of (A). (C) Visual representation of ECM chamber being perfused with NBs, as seen via ultrasound. (D) Collagen I matrix and luminal channel as seen from a top-down view; imaged using light microscopy.

Scanning Electron Microscopy (SEM)

Samples of collagen I matrix were prepared according to the manufacturer's instructions and dehydrated overnight. The samples were then sputtered for 60 s (~8 nm thickness) with palladium in a Denton Vacuum Desk IV Cold Sputter/Etch Unit. A Thermo Fisher Apreo 2S equipped with

Thermo Fisher UltraDry EDS detector was used for SEM imaging. Thermo Fisher Pathfinder Alpine software package was used for analysis (**Supplemental Fig. 1B-D**).

Small Diameter Nanobubble Preparation

Small diameter nanobubbles (S-NBs) were prepared via mechanical agitation as previously described by de Leon et al. (34). The phospholipids 1,2-dipalmitoyl-sn-glycero-3-phospho-ethanolamine (DPPE) and 1,2-dipalmitoyl-sn-glycero-3-phosphate (DPPA) were obtained from Corden Pharma (Liestal, Switzerland); 1,2-distearoyl-snglycero-3-phosphoethanolamine-N- [methoxy(polyethylene glycol)-2000] (DSPE-mPEG 2000) from Laysan Lipids (Arab, AL); and 1,2-dibehenoyl-sn-glycero-3-phosphocholine (DBPC) from Avanti Polar Lipids Inc. (Pelham, AL). DBPC, DPPE, DPPA, and DSPE-mPEG 2000 were dissolved in propylene glycol (Sigma Aldrich; Milwaukee, WI) via sonication bath and heating at 80°C. A solution of glycerol (Acros Organics) and PBS (Gibco, Life Technologies) was heated at 80°C and added to the lipid solution. 1 mL of the solution was sealed in a 3 mL headspace vial with a rubber stopper, and sealed with an aluminum cap. The solution was stored at 4°C until use. The air gas inside the vial was replaced with C_3F_8 gas by purging the vial with 10 mL of C_3F_8 gas (AirGas; Cleveland, OH). S-NBs were activated via agitation in a VialMix mechanical shaker (Bristol-Meyers Squibb Medical Imaging, Inc.; N. Billerica, MA) and isolated via centrifugation (50 g for 5 minutes). As reported in prior studies, S-NBs had a concentration of ~4.07×10^{11} bubbles/mL and diameter of 275 ± 8 nm, as obtained via resonant mass measurement (RMM, Archimedes, Malvern Panalytical Inc., Westborough, MA) and dynamic light scattering (DLS) (**Supplemental Fig. 2A-B**) (34,35). S-NB morphology has been previously investigated using SEM, TEM, and cryo-EM (31,35–38). S-NB lipid structure, shell morphology, and zeta potential have also been previously characterized (34,39).

Large Diameter Nanobubble Preparation

Large diameter NBs (L-NBs) with the same lipid shell composition as the S-NBs were prepared according to Abenojar et al. (38). Briefly, the L-NBs were isolated by diluting the bubble solution obtained after mechanical agitation with a VialMix with 10% vol/vol glycerol/propylene glycol in PBS. They were then centrifuged at 300 g for 10 minutes after which the infranatant was discarded. Next, the remaining L-NB solution was re-dispersed in PBS and centrifuged at different sequential speeds (30, 70, 160, and 270 g) for 1 minute each, after which the infranatant was collected. The infranatant solution was centrifuged at 300 g for 10 minutes and the subsequent infranatant was discarded. The remaining sample was re-dispersed in a solution of 10% vol/vol glycerol/propylene glycol in PBS. The desired L-NB sample (mean diameter = 875 ± 280 nm, mode diameter = 954 ± 20 nm, concentration = 1.18 x 10^{10} bubbles/mL; measurements obtained in previous studies) (representative RMM results can be found in **Supplemental Fig. 2C**) was then transferred to a 3 mL headspace vial, capped with a rubber septum, and sealed with an aluminum cap (38). The vial was then flushed with 10 mL of C_3F_8 gas and used immediately for imaging.

Polystyrene Beads

Microscale and nanoscale polystyrene beads were perfused through the microfluidic chip lumen and imaged with B-mode imaging. According to the manufacturer (Spherotech; Lake Forest, IL), the microscale beads (BP-60-5) had a mean diameter of 6.32 μm and a concentration of 7.21 x 10^7 particles/mL. According to the manufacturer (Polysciences, Inc; Warrington, PA), the nanoscale beads had a mean diameter of 510 ± 8 nm and concentration of 3.64 x 10^{11} particles/mL. Bead concentrations were undiluted for all experimental results. TIC results were analyzed with VevoLab software and normalized by dividing by 5000 for comparison to the grayscale analysis in other experiments. The ROI included the entire matrix below the lumen.

Plasma and RBC Solution Preparation

De-identified venous blood samples were drawn from non-anemic healthy control subjects into heparin containing vacutainers at University Hospitals Cleveland Medical Center (UHCMC) in Cleveland, Ohio under Institutional Review Board (IRB)-approved protocols (05-14-07C). Informed consent was obtained from all study participants. The blood samples were stored at 4 °C until tested. All experiments in this study were performed within 8 h of venipuncture. Blood samples were centrifuged at 500 G for 5 minutes. The red blood cell (RBC) and plasma layers were separated to prevent clotting because the microfluidic matrix is made from collagen, which can trigger the extrinsic coagulation cascade. The plasma layer was removed for use, the buffy coat was aspirated, and the remaining RBCs were rinsed with an equal volume of PBS. The RBC-PBS solution was centrifuged at 500 G for 5 minutes and the PBS layer was removed. This wash cycle was repeated two more times. For experimental studies, plasma was diluted with PBS to 55% plasma (physiological concentration). RBCs were diluted with PBS to 20% RBCs (physiological concentration is 45%). This dilution was chosen due to the high viscosity of RBCs.

Ultrasound Imaging Setup

Imaging was performed with a Vevo 3100 VisualSonics ultrasound using an MX250 transducer (15-30 MHz) with a center transmit frequency of 21 MHz. A transmit frequency of 18 MHz was used for NLC experiments. All experiments were imaged at 5 frames per second (fps) using the nonlinear contrast (NLC) mode with a contrast gain of 30 dB, B-mode gain of 28 dB, dynamic range of 40 dB, and medium beamwidth. Continuous imaging experiments were conducted with 20% power in NLC mode to prevent NB destruction. “Terminal imaging” (i.e., imaging with ultrasound only after the perfusion portion of the experiment concludes) experiments were conducted with 50% power in NLC mode. This higher power was chosen because the microfluidic devices used for these experiments had lids of approximately 2 mm, which require a higher power to image than lids with a thickness closer to 1.5 mm due to attenuation of the incident

waves. The focus was aligned to the bottom wall of the chip, below the matrix. 1 mL solutions of S-NBs (2.03 x 10^{10} S-NBs/mL) or L-NBs (1.18 x 10^{7} L-NBs/mL) in PBS or plasma were perfused through the channel at 50 µL/min using a Fusion 200-X syringe pump (Chemyx; Stafford, TX). RBC experiments were perfused at 20 µL/min due to the higher viscosity of the solution. B-mode images were acquired at the same time as the NLC images (**Supplemental Fig. 3**). B-mode images were acquired with the same parameters as NLC images (18 MHz transmit frequency, 5 fps, 30 dB contrast gain, 28 dB gain, and % power corresponding to experiments).

Continuous and Terminal Imaging Setups

Image acquisition was carried out for 5100 frames (1020 s) for most experiments. For the "continuous imaging" protocol, images were acquired at 5 fps and 20% power. The number of frames was selected as the approximate maximum due to memory constraints. After 1020 s, plain PBS (i.e., no bubbles included) was perfused through the channel to flush away loose bubbles. Flushing out loose bubbles was conducted to ensure that the final signal within the matrix was not being obscured through attenuation or artifacts by the bubble-generated signal in the channel. After approximately 30 s, the device was imaged again and the post-flush contrast intensity was obtained. All plasma and RBC experiments were performed with these ultrasound parameters. For the "terminal imaging" protocol, a baseline before the entrance of NBs was obtained at 50% power and 5 fps. NBs were perfused through the channel without ultrasound imaging for 1020 s. After 1020 s, the channel was flushed with PBS for approximately 30 s, the ultrasound was turned on, and the post-flush contrast intensity was obtained. Videos were extracted as mp4 files and reformatted into matrices using grayscale data for analysis in MATLAB R2020b.

Time-Intensity Curve Analysis

Grayscale analysis was used to create a time-intensity curve (TIC) of NBs in the collagen matrix. Videos were analyzed pre-flush and post-flush with separate regions of interest. The pre-

flush region of interest (ROI) of continuous imaging experiments was the entire matrix below the channel. This was true for both NLC and B-mode images, which were acquired at the same time during imaging. The post-flush ROI of continuous and terminal imaging experiments was the entire matrix, including the channel and matrix above the channel. This was done because after flushing the channel, attenuation from NBs in the channel decreased and NBs that extravasated into the matrix above and below the channel became more visible. Slope data was calculated for continuous imaging experiments with linear regression. For the penetration depth analysis, the maximum penetration depth was identified as the farthest depth in the matrix that NB-generated contrast reached over the course of the experiment. Slopes and the 95% confidence interval were calculated using simple linear regression (GraphPad Prism).

Percent Area of Matrix with Contrast

ImageJ was used to analyze the matrix below the lumen to find the total area of the matrix that included nonlinear NB-generate signal. This analysis was conducted for continuous imaging experiments for S-NBs in solutions of PBS, plasma, and RBCs. Still images were chosen from the conclusion of each experiment (~1020 s). The images were converted to 16-bit and thresholded at a minimum value of 10 to decrease background signal. An ROI was drawn for the entire matrix below the channel and the percent area with signal was calculated from ImageJ software.

Autocorrelation Analysis

An autocorrelation analysis of the time-intensity curve was performed using MATLAB R2020b with the *xcorr()* function. Decorrelation time was defined as the time shift required for the autocorrelation coefficient to reach 0.5 (40,41). Analysis was conducted for continuous imaging experiments with both S-NBs and L-NBs. For each reported data point, approximately 10 adjacent pixels from the same depth were taken as the ROI. Individual pixel decorrelation time was

measured and then averaged with the adjacent pixels. The region of the matrix below the channel was split into three equal sections by matrix depth and ROIs in each section were analyzed at 50, 300, and 900 s. Each time point was analyzed for 200 frames of imaging. Autocorrelation coefficient values were calculated using MATLAB. The decorrelation time map was generated based on the method developed by Wegierak et al. (42). Briefly, the autocorrelation function in MATLAB was used with a decorrelation threshold of 0.5. This was performed for each pixel in the dataset to produce a map of decorrelation time at each spatial location.

Results

3D Microfluidic Chip

Disease states that involve pathological vasculature, especially within the tumor microenvironment, often have highly heterogeneous vasculature, which presents a major challenge in designing effective drug delivery vehicles. NB kinetics are typically studied *in vivo*, but it can be difficult to isolate parameters related to extravasation due to the complexity of the tumor micro-environment. Our team has developed a microfluidic device with a lumen and ECM to characterize these extravasation-related parameters *in vitro*. This device features a collagen I ECM chamber with a lumen extending through the center (**Fig. 1A**). A key feature of this device is that the top and bottom layers are made of PDMS for ultrasound compatibility (**Fig. 1B-C**) (21–23). Collagen concentrations of 2 and 4 mg/mL were used to form the ECM in these chips, corresponding to 3.7 ± 1.5 μm and 1.3 ± 0.7 μm respectively (43). An illustration of what the microfluidic chip would look like under ultrasound imaging is depicted in **Fig. 1C**. Light microscopy images of the ECM and lumen taken from an aerial view are included for comparison to ultrasound images (**Fig. 1D**). When imaged with SEM, the pore sizes correspond to those published in the literature (**Supplemental Fig. 1B-D**).

Continuous Imaging

S-NBs and L-NBs were perfused through the lumen of the microfluidic chip to investigate differences in extravasation and diffusion based on matrix pore size and bubble diameter. L-NBs are used as intravascular contrast agents and one of their advantages is that they do not extravasate. For this study, L-NBs act as a control. Solutions were perfused through the channel at 50 µL/min and continuously imaged under NLC mode ultrasound at 5 fps, 20% power, and 18 MHz transmit frequency. The ROI for this analysis was the entire matrix below the channel and the slope was calculated through linear regression. We found that for S-NBs, the initial wash-in (depicted as "1" on **Fig. 2A**) to the matrix was 2.1x faster for the larger pore size (3.7 µm pores)

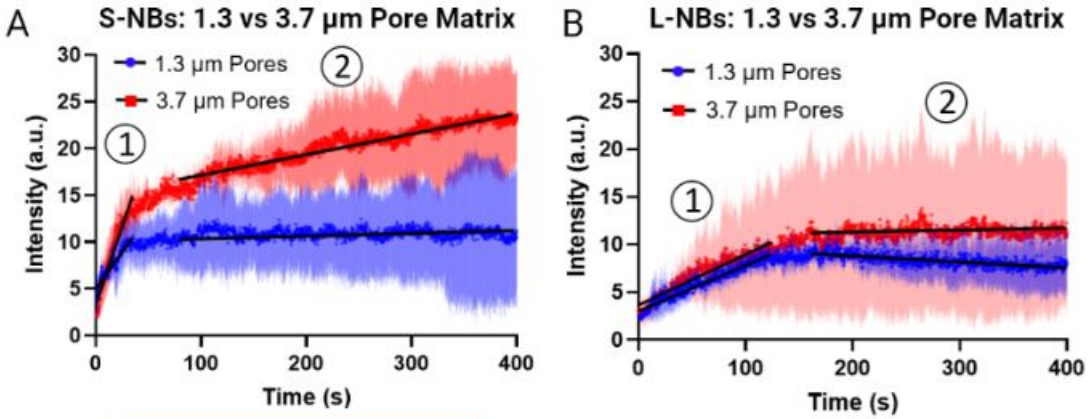

C

	S-NBs	
	1.3 µm Pores	3.7 µm Pores
Slope ①	0.16	0.33
Slope ②	0.00093	0.024
	L-NBs	
	1.3 µm Pores	3.7 µm Pores
Slope ①	0.048	0.053
Slope ②	-0.0061	0.00026

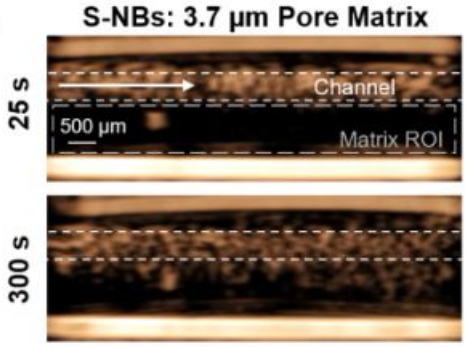

Fig. 2. Continuous imaging time-intensity curve (TIC) and slopes. (A) S-NB and (B) L-NB TICs of grayscale intensity in the matrix (n=3). 1 corresponds to the initial wash-in slope and 2 to the post-wash-in slope. (C) Slope of the TIC during the wash-in to the matrix and post-wash-in. (D) Representative images of S-NBs in a 3.7 µm pore size matrix at 25 and 300 s. The ROI corresponding to **Fig. 2A-B** is denoted.

than the smaller pore size (1.3 μm pores) (**Fig. 2A, C**). Post initial wash-in (depicted as "2" on **Fig. 2A**), S-NBs diffused 25x faster through the 3.7 μm pores (**Fig. 2C**). A representative image of the matrix at 25 and 300 s can be seen in **Fig. 2D**. When L-NB solutions were perfused through the lumen (**Fig. 2B-C**), the initial wash-in slope was 1.1x greater for the 3.7 μm pore matrix. For the post wash-in slopes, both pore sizes had slopes of approximately zero, but the 1.3 μm pore slope was negative while 3.7 μm pore slope was positive.

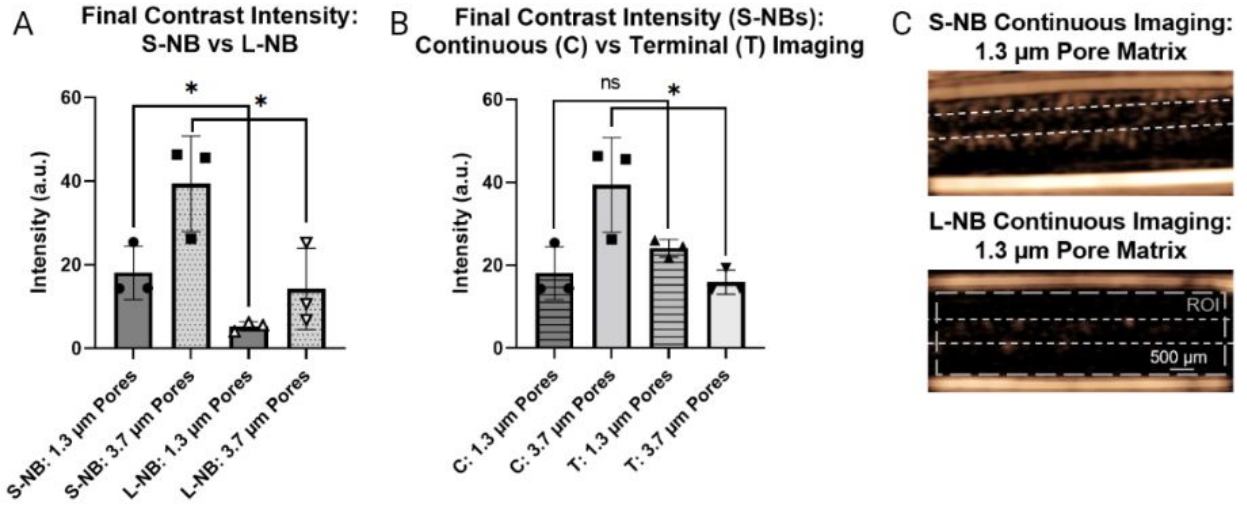

Fig. 3. Non-linear contrast (NLC) intensity in the matrix after channel flush with PBS. (a) Continuous imaging comparison between S-NBs and L-NBs (n=3). (b) Continuous vs terminal imaging of S-NBs (n=3). (c) Representative images of the matrix after wash-out. The region of interest (ROI) is denoted in gray. The channel boundaries are indicated in white. * indicates $p<0.05$. Bars represent standard deviation.

Matrix Intensity Post-Channel Flush

After 5100 frames of imaging, the matrices were flushed with PBS for approximately 30 s and then imaged again to analyze leftover contrast in the matrix. This flush was done to ensure that the NLC signal within the matrix was due to bubbles stuck within the matrix as opposed to signal within the channel. ROIs were taken as the entire matrix, including the channel. When continuous imaging experiments were compared between S-NBs and L-NBs, the S-NB matrices had significantly greater remaining contrast compared to the L-NBs at both 3.7 μm (S-NB: 39.4 ±

11.4 a.u.; L-NB: 14.3 ± 9.8 a.u.) and 1.3 μm (S-NB: 18.1 ± 6.4 a.u.; L-NB: 5.3 ± 1.1 a.u.) matrix pore sizes (**Fig. 3A**). Representative images can be seen in **Fig. 3C**.

Terminal imaging experiments were conducted to determine if ultrasound waves were increasing NB accumulation within the matrix. When comparing continuous imaging to terminal imaging (i.e., perfusing S-NBs through the channel for 1020 s without imaging and then imaging post-flush) results with S-NBs, there was a significant difference for the 3.7 μm pore size matrix (continuous: 39.4 ± 11.4 a.u; terminal imaging: 24.2 ± 2.1 a.u.), but not for the 1.3 μm pore size matrix (continuous: 18.1 ± 6.4 a.u.; terminal imaging: 15.9 ± 2.9 a.u.) (**Fig. 3B**). We hypothesize that this indicates that S-NB extravasation is more affected by ultrasound-related effects like acoustic radiation force when pore sizes are large.

Penetration Depth

Maximum penetration depth was analyzed to account for the heterogeneity of the pore sizes in the matrix (**Fig. 4A-B**). Maximum penetration depth is defined here as the maximum depth below the channel that S-NB-generated contrast reaches during the experiment (**Fig. 4D**). Differences were calculated using unpaired t-tests. When S-NBs in different pore size matrices were compared during continuous imaging experiments, there was a significant difference (1.3 μm: 0.50 ± 0.032 mm; 3.7 μm: 0.69 ± 0.019 mm). However, there was no significant difference for L-NBs (1.3 μm: 0.25 ± 0.091 mm; 3.7 μm: 0.49 ± 0.13 mm) (**Fig. 4A**). Note that the standard deviation for L-NBs is 3-7x greater than for S-NBs. S-NBs had a significantly greater penetration depth than L-NBs with 1.3 μm pores, but not for the 3.7 μm pores.

When penetration depth was compared between large and small pore matrices for terminal imaging experiments (**Fig. 4B**), S-NBs penetrated 1.3x deeper into the larger pore size matrix (1.3 μm: 0.32 ± 0.049 mm) than the smaller pore size (3.7 μm: 0.42 ± 0.038 mm). There was a significant difference between continuous and terminal imaging experiments at both matrix concentrations.

S-NBs were also perfused through the microfluidic chip in solutions of RBCs and plasma. Using ImageJ, the region of the matrix below the channel was analyzed to find the percent of that region that included S-NB-generated contrast (**Fig. 4C**). RBCs had the largest area with nonlinear signal (85.2 ± 13.0 %), followed by PBS (67.7 ± 17.9 %) and then plasma (54.9 ± 14.5 %). A visual representation of S-NBs in a solution of RBCs at t = 0 and 800 s can be seen in **Fig. 4E**.

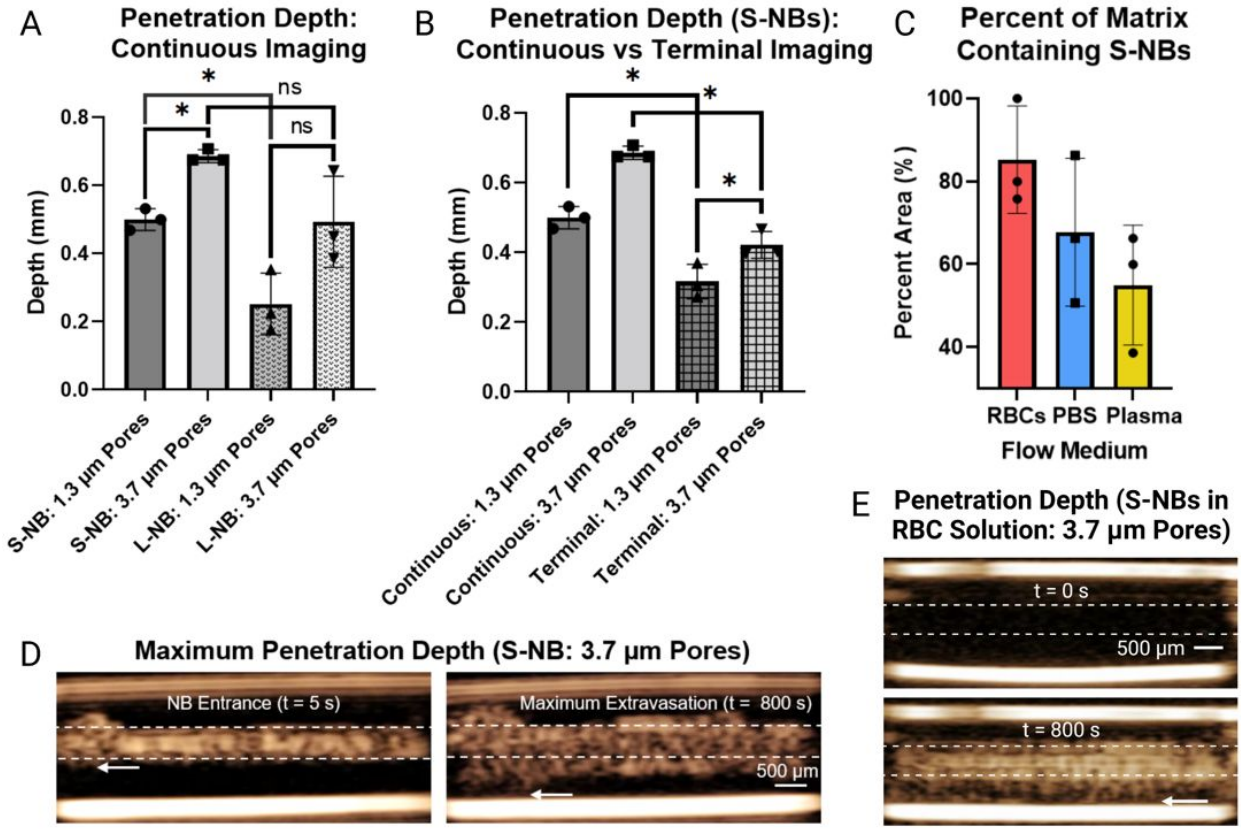

Fig. 4. Maximum penetration depth of S-NBs and L-NBs into the matrix. (A) Continuous imaging of S-NBs vs L-NBs (n = 3). (B) Continuous vs terminal imaging of S-NBs (n = 3). (C) Percent of the 3.7 µm pore matrix below the channel that contains contrast after ~1020 s for S-NBs in RBC, plasma, or PBS solutions. (D) Visual representation of penetration depth at t = 5 s compared to t = 800 s. (E) Representative image of NLC of NBs in an RBC solution at 0 and 800 s. The arrow denotes the maximum depth of contrast. The channel boundaries are indicated in white. * indicates $p < 0.05$. Bars represent standard deviation.

Autocorrelation Analysis

Autocorrelation can provide insight into patterns of NB movement through an ROI. A single pixel is taken as the ROI and the initial frame of imaging is compared to subsequent frames. Decorrelation time is defined as the time-shift for the correlation coefficient to reach 0.5 (40,41).

Non-zero decorrelation time indicates that there is a pattern between imaging frames. We used this analysis to differentiate flowing bubbles from bubbles that are slowly diffusing through the matrix.

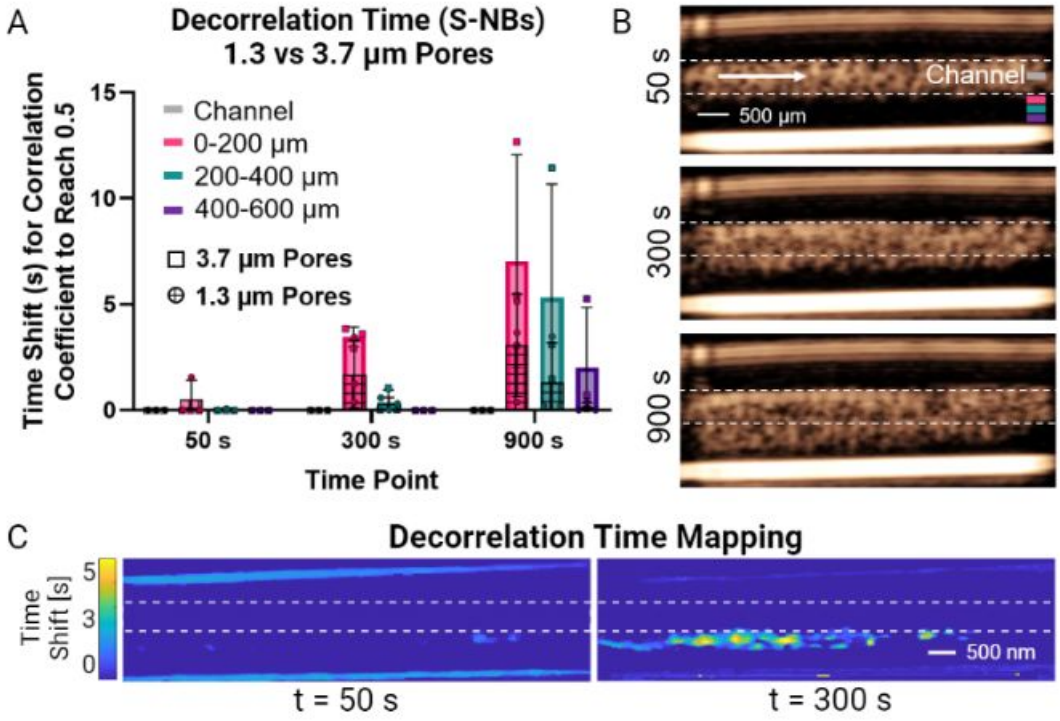

Fig. 5. Autocorrelation analysis. (A) Decorrelation time of S-NBs in 1.3 vs 3.7 µm pore matrices. The 3.7 µm pore matrix shows an extended decorrelation time compared to 1.3 µm pore matrix at all time points. (B) Visual representation of time points in the 3.7 µm pore matrix. Rectangles that are color corresponding to **Fig. 5A** (matrix depth) are denoted. (C) Maps of decorrelation time in the microfluidic chip by pixel at t = 50 s and 300 s, based on a technique developed by Wegierak et al. (42). The channel boundaries are indicated in white. Bars represent standard deviation. For all experiments, n=3.

Decorrelation time was analyzed in the channel, 0-200 µm away from the channel, 200-400 µm away from the channel, and 400-600 µm away from the channel at 50, 300, and 900 s after the entrance of S-NBs to the channel (**Fig. 5A-B**). This analysis was conducted for S-NBs with continuous imaging in matrices with 1.3 and 3.7 µm pore sizes. Within the channel, decorrelation time was zero seconds at all time points. As imaging time increased, ROIs closest to the channel began to show extended decorrelation time and at 900 s, all sections of the matrix showed an extended decorrelation time in the 3.7 µm pore size matrix. This extended decorrelation time at

900 s was most substantially seen in the section of the matrix closest to the channel (0-200 μm: 7.1 ± 5.0 s; 200-400 μm: 5.3 ± 5.3 s; 400-600 μm: 2.0 ± 2.8 s). For the 1.3 μm pore size matrix, all mean values were lower than the 3.7 μm pore size matrix (0-200 μm: 3.1 ± 2.4 s; 200-400 μm: 1.3 ± 1.9 s; 400-600 μm: 0.13 ± 0.22 s). A visual representation of decorrelation time at each spatial location in the dataset can be seen in **Fig. 5C** with time points (t = 50 and 300 s) corresponding to the graph in **Fig. 5A**. L-NBs did not show an extended decorrelation time at any section of the matrix with the 1.3 μm pore size matrix and minimal extended decorrelation time with 3.7 μm pores (**Supplemental Fig. 4**).

B-mode Imaging of S-NBs

A comparative analysis between B-mode and NLC imaging was conducted to expand the application of this study from NBs to, more broadly, nanoparticles that are not readily visible under NLC. During NLC acquisition, B-mode images were acquired at the same time under the same conditions (e.g., frame rate, transmit frequency) as NLC images. On TIC analysis (n=3) of the 3.7 μm pore size matrix, over the first 200 s of imaging, B-mode images showed less sensitivity than NLC images with an average standard deviation of 4.4 ± 1.4 a.u. while NLC images had a standard deviation of 1.9 ± 1.0 a.u. (**Fig. 6A, C**). B-mode imaging was less sensitive than NLC imaging, but the matrix TIC results still showed an increase in intensity over time during continuous imaging. Decorrelation time was compared for a single 3.7 μm pore size matrix experiment and again, B-mode was less sensitive than NLC mode (**Fig. 6B**). However, B-mode still showed an extended decorrelation time at 900 s in all three sections of the matrix.

B-mode Imaging of Polystyrene Beads

Polystyrene beads were perfused through the microfluidic chip lumen to determine if non-bubble particles could be visualized with B-mode imaging. 500 nm beads showed an increase in signal intensity until approximately 200 s of imaging (**Fig. 6D**). There was a 10.6x increase in the

average signal intensity from baseline to the peak. This is reflected visually in **Fig. 6E**. In comparison, 6 µm polystyrene beads had a 1.3x increase in signal intensity. The 6 µm bead was used as a control because the beads would not be able to extravasate or move beyond the area directly adjacent to the channel.

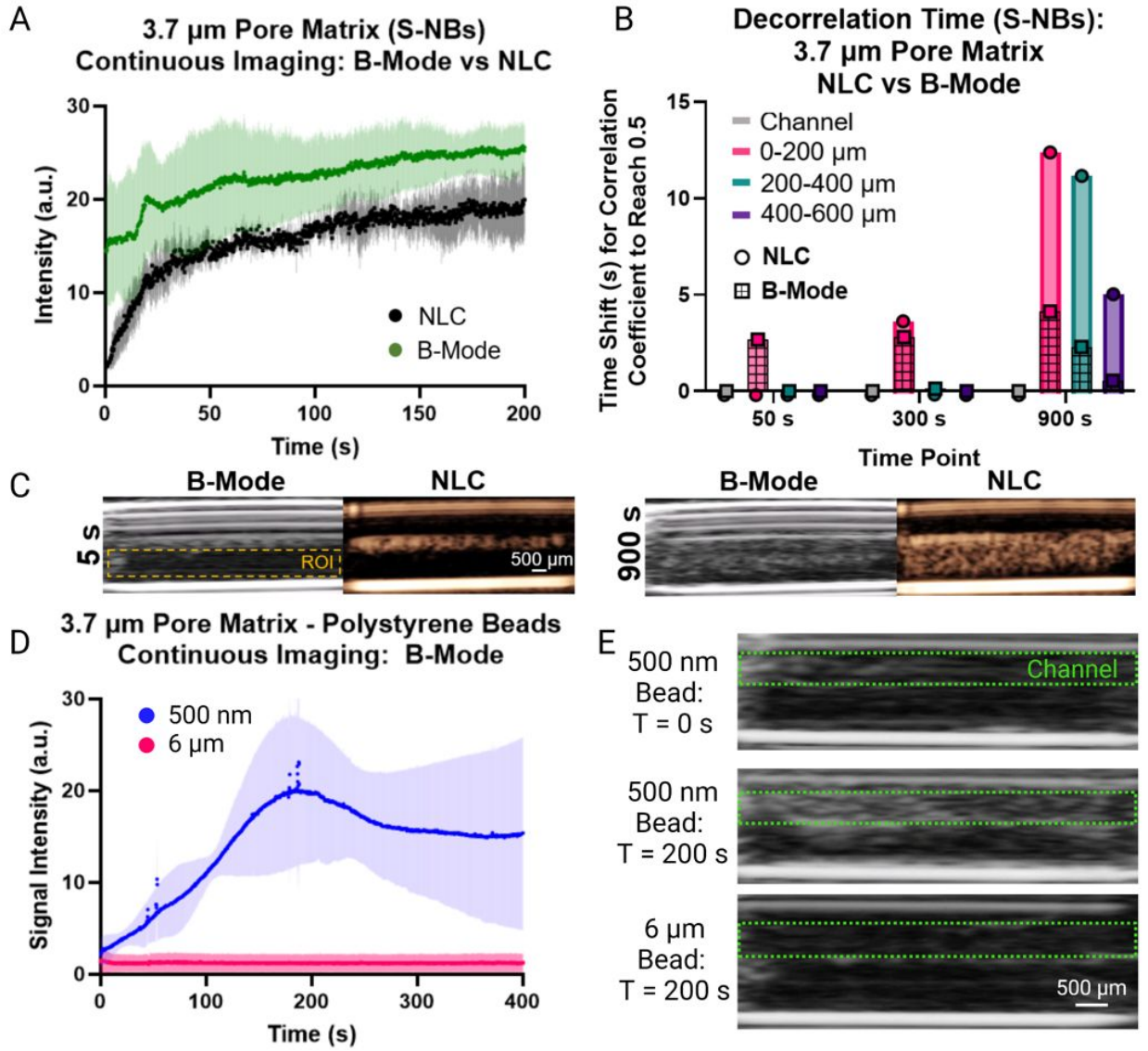

Fig. 6. B-mode vs non-linear contrast (NLC) imaging with S-NBs and polystyrene beads. (A) TIC. B-mode imaging is less sensitive, but still showed an increase in grayscale intensity over time (n=3). (B) Decorrelation time. Less sensitivity with B-mode than NLC mode, but B-mode still showed an increase in decorrelation time over the entire matrix over time. (C) Visual representation of B-mode and NLC mode images at 5 and 900 s. (D) Signal intensity of the matrix over time when 500 nm and 6 µm beads are flown through the lumen, analyzed from B-mode

images (n=3). (E) Visual representation of the matrix B-mode signal intensity of 500 nm and 6 μm beads at baseline or 200 s after flow began.

Discussion

Successful nanoparticle-based therapeutics and imaging agents in pathologies involving pathological vasculature, especially within oncology, are dependent on many factors, including the effectiveness of margination, extravasation, tissue penetration, and retention in the tissue (44,45). The characteristics of the nanoparticles themselves (e.g., diameter, shape, stiffness, targeting) can help or hinder their path to their target site (11,46–49). This study leverages a tunable microfluidic platform to characterize the extravasation of nanoparticles and their penetration depth in real-time, with a field of view that is significantly larger than standard microscopy methods (12–14,50,51). The large field of view afforded by this model is essential to accurately capture heterogeneous microenvironments, such as that which occurs in tumors and other chronic inflammatory conditions.

To our knowledge, using ultrasound to image nanoparticle extravasation into and diffusion through an ECM in a microfluidic device has not been previously reported. This model uses collagen type I concentrations of 2 and 4 mg/mL, corresponding to 3.7 ± 1.5 μm and 1.3 ± 0.7 μm pores, respectively (43). While these pore sizes are larger than the endothelial gaps in most pathologies, some mammary carcinomas have functional pore sizes of 1.2-2 μm, corresponding to the 4 mg/mL collagen concentration matrix (52,53). It has been reported that an ECM pore size of 1-3 μm facilitates tissue-invasive behavior of cancer cells (52,54). This is in agreement with both matrix pore sizes (**Supplemental Fig. 1B-D**). Due to the tunability of this device for many applications, groups interested in smaller pore sizes could use a higher concentration of collagen, other ECM-based materials, or they could add a permeabilizable endothelial cell layer around the lumen (55).

One of the principal advantages of using ultrasound over other imaging modalities (e.g., confocal and two-photon microscopy) to visualize and quantify extravasation within a microfluidics

model is its ability to image in real-time with a large depth of penetration (dependent on the ultrasound frequency), and a wide field of view (56). There is a loss of resolution with ultrasound compared to microscopy, but this is balanced by the wide field of view, which is required to appreciate the heterogeneity within the ECM and improve aspects of translation to *in vivo* models (57–59). Resolution can be improved by using higher ultrasound frequencies, but maximum penetration depth decreases with increasing frequency. In this work, the field of view was chosen to fit the size of the microfluidics chip (approximately 8 mm x 10 mm for B-mode imaging). The maximum field of view of the system was not reached, leaving open the option for larger setups in the future.

Four primary parameters were tested with NBs flowing through the microfluidic chip: 1) contrast intensity over time with continuous imaging; 2) contrast intensity after the channel is flushed with PBS; 3) penetration depth of contrast; and 4) decorrelation time. NBs produce contrast, seen in NLC imaging, and to apply this study and method to other non-contrast capable nanoparticles, parameters 1 and 4 were also analyzed with B-mode imaging.

When S-NBs were perfused through matrices with large and small pore sizes (**Fig. 2A**), the wash-in slope of S-NBs into the larger pore matrix was approximately 2x greater than the smaller pore matrix. We hypothesize that wash-in behavior is governed by the pores adjacent to the channel where S-NBs fill those spaces quickly, but take a longer time to diffuse through the remaining matrix. After the initial wash-in, the slope of the larger pore matrix became 25x greater than the smaller matrix slope.

When L-NBs were perfused through the matrices, the wash-in slope and post wash-in slope were approximately the same for both concentrations with the larger pore matrix having a slightly greater slope in both cases (**Fig. 2B**). When compared to S-NBs, the maximum intensity was significantly less for L-NBs. However, it must be noted that the concentration of S-NBs was approximately three orders of magnitude greater and the gas volume was approximately two orders of magnitude greater than L-NBs. The concentrations were chosen to maximize contrast

intensity in the microfluidic chip under ultrasound before attenuation was reached. *In vivo*, maximum contrast intensity before attenuation onset is often desired. In this study, the L-NB diameter had a mode of approximately 1 μm and a mean of 875 nm (38). S-NB and L-NB diameters were found using dynamic light scattering (DLS) and resonance mass measurement (RMM, Archimedes) techniques (**Supplemental Fig. 2**) (34,35,38). The mean L-NB diameter was approximately $^2/_3$ and $^1/_4$ of the smaller and larger mean matrix pore diameters respectively. S-NBs had diameters that were approximately $^1/_5$ and $^1/_{10}$ of the mean matrix pore diameters. It is noteworthy that the standard deviation for the larger pore matrix concentration was significantly larger than the smaller pore matrix. We hypothesize that the heterogeneity of the matrix has a more significant impact on extravasation and diffusion with larger nanoparticles and microparticles than with smaller nanoparticles (<500 nm diameter). Microparticles have a greater probability of getting lodged in a heterogeneous matrix in areas with smaller pore sizes and vice versa.

It must also be noted that this experiment was conducted at 5 fps. It is well known that when UCAs (i.e., MBs and NBs) are continuously imaged under ultrasound, their signal decays due to gas dissipation from ultrasound-induced oscillations (60). Thus, the true concentration of bubbles, or leftover lipid from the bubble shell, within the matrix is likely greater than is indicated because some of the bubbles have experienced signal decay. They are no longer contributing to the increase in intensity in the matrix over time. If this phenomenon was not occurring, the L-NB and S-NB slopes and final intensities may have a greater magnitude.

When channels were flushed with PBS after the continuous imaging experiments, to highlight only extravasated bubbles, there was a statistically significant difference between S-NBs and L-NBs at both matrix concentrations (**Fig. 3A**). A major advantage of MBs, or larger NBs, for clinically approved applications is that they are intravascular agents and they should not extravasate; thus, these results are expected and showcase the different uses of S-NBs and L-NBs. More S-NBs were visible in the matrix and adjacent to the channel than L-NBs, visually depicted in **Fig. 3C**. Maximum penetration depth was also compared and there was a statistically

significant difference between S-NBs at the two matrix concentrations where S-NBs penetrated 1.3x deeper into the matrix with the larger pore size (**Fig. 4B**). S-NBs also penetrated 2x more deeply into the smaller matrix than L-NBs. However, there was no statistically significant difference between S-NBs and L-NBs with the larger pore size matrix or between the two matrix concentrations with L-NBs. Again, this may be because the heterogeneity of the matrix is more impactful on the probability of extravasation of larger particles. This theory is supported by the significantly larger standard deviation in contrast intensity between experiments with L-NBs than S-NBs.

When post-flush contrast intensity for continuous imaging and terminal imaging experiments (S-NBs only) were compared (**Fig. 3B**), there was a significant difference between the signal intensity in matrices with a large pore size, but not a small pore size. We hypothesize that this is because acoustic radiation force (force pushing NBs in the direction of the ultrasound-generated sound wave) plays a larger role in matrices with a larger pore size. This effect may be because acoustic radiation force can push a greater concentration of NBs into large pores in the matrix adjacent to the channel lumen, improving the probability for their diffusion through the matrix. Acoustic radiation force may also play a role in improving NB penetration through the matrix. The final contrast intensity and penetration depth of NBs in continuous imaging experiments is likely dependent on both diffusive and acoustic radiation forces. There has been research with MBs and nanoparticles on the role of acoustic radiation force in improving the targeting of specific tissues, such as the tumor microenvironment (61–64). Acoustic radiation force increases the likelihood that NBs reach the lumen wall in both matrix concentrations, improving the probability of diffusion. However, diffusion through a smaller pore size is more difficult, contributing to a decrease in contrast intensity.

S-NBs in solutions of PBS, RBCs, or plasma were also compared to see the effect of the flow medium on extravasation and diffusion through the matrix (**Fig. 4C**). The analysis identified total coverage of the matrix below the channel that contained NB-generated nonlinear signal.

Studies have shown that the presence of RBCs in a flow medium can change margination dynamics by making margination less random, especially for particles with a diameter > 200 nm (S-NB diameter = ~ 200-400 nm) (47). Other studies have indicated that for particles smaller than a red blood cell, their margination is enhanced by collisions with RBCs and flow shear (65,66).This could explain why in this study, there was more NB-generated signal in the matrix for the RBC group than PBS or plasma. This is reflected by the representative images in PBS (**Fig. 4D**) and RBCs (**Fig. 4E**). In this experiment, the chosen hematocrit was 20% in order to increase in viscosity in adding RBCs to the flow medium. The observed effects could be augmented if the hematocrit was increased to the physiological concentration of 45%. Bubbles in plasma showed the least signal in the matrix. We hypothesize that this is due to the interaction of plasma proteins with the collagen matrix, which may cause a volume exclusion effect, hindering NB extravasation (67). There is also evidence that plasma proteins interact with the nanoparticles themselves, even if they are PEGylated, implying that nanoparticle extravasation kinetics are affected by the presence of plasma (68–70). Thus, the presence of RBCs or plasma play a role in the dynamics of nanoparticle extravasation, and hence diffusion, through the collagen matrix.

Penetration depth of bubbles was greatly dependent on the heterogeneity of the collagen matrix (**Fig. 4B**). When continuous and terminal imaging experiments were compared, there was a significant difference between the experimental types at both matrix concentrations. This further expounds the role of acoustic radiation force in addition to factors like shear flow, where studies have shown that particle margination is dependent on shear rate (47,71). Regardless, even without acoustic radiation force, S-NBs marginate to and diffuse through the matrix at both collagen concentrations (**Figs. 3-4)**. In the future, imaging at a slower frame rate, such as 1 fps, would be of interest. A slower imaging rate could provide enough acoustic radiation force to improve margination and extravasation of the S-NBs, while dissipating the S-NB agents at a reduced rate.

The difference in stiffness of the matrix between the two collagen concentrations may also affect the extravasation and diffusion of the NBs. As the collagen concentration increases, the stiffness of the matrix also increases, which could decrease the diffusion rate. This has been shown in other studies on nanoparticle delivery efficiency through an ECM (72). Due to this microfluidic device's tunable properties, adaptations of this setup could be used to study barriers to extravasation and diffusion such as stiffer matrices (e.g., different materials for the matrix or cross-linking) or a permeabilizable endothelium.

It should be noted that terminal imaging experiments used 50% power as opposed to the 20% power used for the continuous imaging experiments. This power was chosen because some of the microfluidic chips had lids closer to 2 mm thickness instead of the desired 1.5 mm. Imaging at 50% power could influence the results by artificially increasing contrast intensity for the terminal imaging experiments, especially because NBs are not being destroyed throughout the experiment. However, continuous imaging experiments still had a greater intensity and depth of penetration. Thus, the increase in percent power could be accurately compensating for the increased lid thickness.

Autocorrelation analysis has previously been used to estimate velocity in power and color doppler imaging, analyze hepatic vasculature, and identify differences between NB movement in PBS versus whole blood (40,73–75). However, to our knowledge, it has not been used with a microfluidic model to identify if nanoparticles are flowing in a vessel versus slowly diffusing through an ECM. We hypothesized that decorrelation time could be used to identify slow-moving NBs and that decorrelation time would only be extended if NBs were in the matrix. We found that as S-NBs diffused through the matrix, decorrelation time increased whereas decorrelation time in the channel where the S-NBs were flowing was consistently zero seconds (**Fig. 5**). This is represented visually in the decorrelation time map in **Fig. 5C**. Decorrelation time could be used to identify NBs that are immobile (e.g., adhered to the vessel wall or a tumor cell) or slow moving (e.g., diffusing through the ECM) versus NBs flowing in vessels. This analysis has a direct impact

on *in vivo* work with tumor imaging in that it could provide insight into the tumor microenvironment without histological analysis.

To expand the application of this study from NBs to other nanoparticles, B-mode images acquired concurrently with NLC images were analyzed and compared to NLC results. B-mode images were less sensitive than NLC images, but they showed the same trend with an increase in grayscale intensity in the matrix over time (**Fig. 6A**). Autocorrelation analysis was compared between B-mode and NLC mode data in a single experiment. Again, B-mode was less sensitive than NLC mode, but decorrelation time was extended over the entire matrix by the final time point (900 s) (**Fig. 6B**). Nanoparticles have been seen under ultrasound when using B-mode imaging in other studies (76,77). However, to confirm that this setup could be used in B-mode with other nanoparticles, polystyrene beads of 500 nm and a control size of 6 μm were perfused through the channel with the same ultrasound parameters as the S-NB experiments. While the flow of the 500 nm particles was not visible in the channel, their accumulation in the matrix was visible with a matrix signal intensity that increased 10.6x greater than baseline intensity. In comparison, the 6 μm beads were visible in the channel, but there was no accumulation in the matrix. Thus, the parameters presented in this work could be applied to nanoparticles with a similar diameter to the S-NBs. This study does not investigate other factors that may influence extravasation such as particle shell stiffness, flow rate, width of the lumen, ultrasound power, or depth of the collagen matrix. However, this setup could be used to study all of the aforementioned parameters with small and easily altered adjustments to the experimental setup.

There are some limitations to this study. S-NB and L-NB experiments had different concentrations, which could skew some comparative results. However, regardless of concentration, it is apparent that large particle size limits diffusion through the matrix. Flow rate and vessel diameter can also be decreased to more closely mimic capillaries and post-capillary venules, which is where most physiological extravasation occurs. While the pore sizes in this study can be compared to cancers that have very large endothelial gaps, they are not necessarily

comparable to all types of tumors or tissues with pathological blood vessels. Thus, there should be exploration into ECMs with more protein complexity.

Conclusion

We developed an ultrasound-compatible microfluidic device through which nanoparticle extravasation kinetics can be observed in a simple, controlled environment. The entire depth and length of the channel and matrix were imaged in real-time using standard ultrasound imaging in B-mode and nonlinear contrast mode. This method provides a straightforward setup for characterization of nanoparticle extravasation, nanoparticle diffusion through the matrix, and autocorrelation analysis to differentiate flowing versus slowly moving NBs. The microfluidic chip setup paired with ultrasound also has potential to be used with a variety of nanoparticles, including those that are not visible under contrast-enhanced ultrasound (e.g., liposomes, solid polymers, etc.). This model can provide valuable insight into the extravasation and diffusion capacity of nanoparticles prior to translation to *in vivo* models.

Acknowledgements

This research was supported by the National Institute of General Medical Sciences (T32GM007250); the National Center for Advancing Translational Sciences (TL1TR000441); the National Heart, Lung, and Blood Institute (T32HL134622, F30HL160111, R01HL133574, and R42HL160384); the National Institute of Biomedical Imaging and Bioengineering (R01EB025741 and R01EB028144); the National Cancer Institute (R21CA253108); and National Science Foundation (NSF) CAREER Award 1552782; and the Harrington Discovery Institute at University Hospitals in Cleveland, OH. The authors would like to acknowledge the support of the staff and use of instruments in the CWRU, Case School of Engineering SCSAM Center for the collection and analysis of SEM data, and the Materials for Opto/Electronics Research and Education Center

for assistance with device fabrication. The authors would like to thank N. M. Cooley for grammatical review and Somin Jung for assistance with device fabrication.

Declaration of Competing Interests

U. A. G. and Case Western Reserve University have financial interests in Hemex Health Inc., BioChip Labs Inc. and Xatek Inc. U. A. G. has financial interests in DxNow Inc. Financial interests include licensed intellectual property, stock ownership, research funding, employment, and consulting. Hemex Health Inc. offers point-of-care diagnostics for hemoglobin disorders, anemia, and malaria. BioChip Labs Inc. offers commercial clinical microfluidic biomarker assays for inherited or acquired blood disorders. Xatek Inc. offers point-of-care global assays to evaluate the hemostatic process. DxNow Inc. offers microfluidic and bio-imaging technologies for in vitro fertilization, forensics, and diagnostics. Competing interests of Case Western Reserve University employees are overseen and managed by the Conflict of Interests Committee according to a Conflict-of-Interest Management Plan.

References

1. Yao Y, Zhou Y, Liu L, Xu Y, Chen Q, Wang Y, et al. Nanoparticle-Based Drug Delivery in Cancer Therapy and Its Role in Overcoming Drug Resistance. Front Mol Biosci. 2020 Aug 20;7.
2. Senapati S, Mahanta AK, Kumar S, Maiti P. Controlled drug delivery vehicles for cancer treatment and their performance. Signal Transduct Target Ther. 2018 Dec 1;3(1).
3. Haley B, Frenkel E. Nanoparticles for drug delivery in cancer treatment. Urologic Oncology: Seminars and Original Investigations. 2008 Jan;26(1):57–64.
4. Anselmo AC, Mitragotri S. Nanoparticles in the clinic: An update. Bioeng Transl Med. 2019 Sep;4(3).
5. Wilhelm S, Tavares AJ, Dai Q, Ohta S, Audet J, Dvorak HF, et al. Analysis of nanoparticle delivery to tumours. Nat Rev Mater. 2016 May 26;1(5):16014.

6. Smith BR, Kempen P, Bouley D, Xu A, Liu Z, Melosh N, et al. Shape matters: Intravital microscopy reveals surprising geometrical dependence for nanoparticles in tumor models of extravasation. Nano Lett. 2012 Jul 11;12(7):3369–77.

7. Lin Q, Fathi P, Chen X. Nanoparticle delivery in vivo: A fresh look from intravital imaging. Vol. 59, EBioMedicine. Elsevier B.V.; 2020.

8. van de Ven AL, Wu M, Lowengrub J, McDougall SR, Chaplain MAJ, Cristini V, et al. Integrated intravital microscopy and mathematical modeling to optimize nanotherapeutics delivery to tumors. AIP Adv. 2012 Mar 1;2(1).

9. Wang Z. Imaging nanotherapeutics in inflamed vasculature by intravital microscopy. Vol. 6, Theranostics. Ivyspring International Publisher; 2016. p. 2431–8.

10. Wu H, Abenojar EC, Perera R, de Leon AC, An T, Exner AA. Time-intensity-curve Analysis and Tumor Extravasation of Nanobubble Ultrasound Contrast Agents. Ultrasound Med Biol. 2019 Sep 1;45(9):2502–14.

11. Perera R, Deleon A, Wang X, Ramamurtri G, Peiris P, Basilion J, et al. Nanobubble Extravasation in Prostate Tumors Imaged with Ultrasound: Role of Active versus Passive Targeting. In: IEEE International Ultrasonics Symposium, IUS. 2018.

12. Pellow C, Abenojar EC, Exner AA, Zheng G, Goertz DE. Concurrent visual and acoustic tracking of passive and active delivery of nanobubbles to tumors. Theranostics. 2020;10(25):11690–706.

13. Vu MN, Rajasekhar P, Poole DP, Khor SY, Truong NP, Nowell CJ, et al. Rapid Assessment of Nanoparticle Extravasation in a Microfluidic Tumor Model. ACS Appl Nano Mater. 2019 Apr 26;2(4):1844–56.

14. Wang HF, Ran R, Liu Y, Hui Y, Zeng B, Chen D, et al. Tumor-Vasculature-on-a-Chip for Investigating Nanoparticle Extravasation and Tumor Accumulation. ACS Nano. 2018 Nov 27;12(11):11600–9.

15. Man Y, Kucukal E, An R, Watson QD, Bosch J, Zimmerman PA, et al. Microfluidic assessment of red blood cell mediated microvascular occlusion. Lab Chip. 2020 Jun 21;20(12):2086–99.

16. Ingber DE. Human organs-on-chips for disease modelling, drug development and personalized medicine. Nat Rev Genet. 2022;

17. Alapan Y, Kim C, Adhikari A, Gray KE, Gurkan-Cavusoglu E, Little JA, et al. Sickle cell disease biochip: a functional red blood cell adhesion assay for monitoring sickle cell disease. Translational Research. 2016 Jul 1;173:74-91.e8.

18. Jasaitiene D, Valiukeviciene S, Linkeviciute G, Raisutis R, Jasiuniene E, Kazys R. Principles of high-frequency ultrasonography for investigation of skin pathology. Journal of the European Academy of Dermatology and Venereology. 2011 Apr;25(4):375–82.

19. Fernandez Rivas D, Kuhn S. Synergy of Microfluidics and Ultrasound: Process Intensification Challenges and Opportunities. Vol. 374, Topics in Current Chemistry. Springer Verlag; 2016.

20. Rademeyer P, Carugo D, Lee JY, Stride E. Microfluidic system for high throughput characterisation of echogenic particles. Lab Chip. 2015 Jan 21;15(2):417–28.

21. Pulsipher KW, Hammer DA, Lee D, Sehgal CM. Engineering Theranostic Microbubbles Using Microfluidics for Ultrasound Imaging and Therapy: A Review. Vol. 44, Ultrasound in Medicine and Biology. Elsevier USA; 2018. p. 2441–60.

22. Strohm EM, Gnyawali V, Sebastian JA, Ngunjiri R, Moore MJ, Tsai SSH, et al. Sizing biological cells using a microfluidic acoustic flow cytometer. Sci Rep. 2019 Dec 1;9(1).

23. Bourn MD, Batchelor DVB, Ingram N, McLaughlan JR, Coletta PL, Evans SD, et al. High-throughput microfluidics for evaluating microbubble enhanced delivery of cancer therapeutics in spheroid cultures. Journal of Controlled Release. 2020 Oct 10;326:13–24.

24. Lin H, Chen J, Chen C. A novel technology: microfluidic devices for microbubble ultrasound contrast agent generation. Med Biol Eng Comput. 2016 Sep 25;54(9):1317–30.

25. Pulsipher KW, Hammer DA, Lee D, Sehgal CM. Engineering Theranostic Microbubbles Using Microfluidics for Ultrasound Imaging and Therapy: A Review. Ultrasound Med Biol. 2018 Dec;44(12):2441–60.

26. Carugo D, Browning RJ, Iranmanesh I, Messaoudi W, Rademeyer P, Stride E. Scaleable production of microbubbles using an ultrasound-modulated microfluidic device. J Acoust Soc Am. 2021 Aug;150(2):1577–89.

27. Abou-Saleh RH, Armistead FJ, Batchelor DVB, Johnson BRG, Peyman SA, Evans SD. Horizon: Microfluidic platform for the production of therapeutic microbubbles and nanobubbles. Review of Scientific Instruments. 2021 Jul 1;92(7):074105.

28. van Elburg B, Collado-Lara G, Bruggert GW, Segers T, Versluis M, Lajoinie G. Feedback-controlled microbubble generator producing one million monodisperse bubbles per second. Review of Scientific Instruments. 2021 Mar 1;92(3):035110.

29. Segers T, de Rond L, de Jong N, Borden M, Versluis M. Stability of Monodisperse Phospholipid-Coated Microbubbles Formed by Flow-Focusing at High Production Rates. Langmuir. 2016 Apr 26;32(16):3937–44.

30. de Leon A, Perera R, Nittayacharn P, Cooley M, Jung O, Exner AA. Ultrasound Contrast Agents and Delivery Systems in Cancer Detection and Therapy. In: Advances in Cancer Research. Academic Press Inc.; 2018. p. 57–84.

31. Exner AA, Kolios MC. Bursting microbubbles: How nanobubble contrast agents can enable the future of medical ultrasound molecular imaging and image-guided therapy. Curr Opin Colloid Interface Sci. 2021 Aug 1;54.

32. Chrobak KM, Potter DR, Tien J. Formation of perfused, functional microvascular tubes in vitro. Microvasc Res. 2006 May;71(3):185–96.

33. Polacheck WJ, Kutys ML, Tefft JB, Chen CS. Microfabricated blood vessels for modeling the vascular transport barrier. Nat Protoc. 2019 May 1;14(5):1425–54.

34. de Leon A, Perera R, Hernandez C, Cooley M, Jung O, Jeganathan S, et al. Contrast enhanced ultrasound imaging by nature-inspired ultrastable echogenic nanobubbles. Nanoscale. 2019;11(33).

35. Abenojar EC, Bederman I, de Leon AC, Zhu J, Hadley J, Kolios MC, et al. Theoretical and experimental gas volume quantification of micro-and nanobubble ultrasound contrast agents. Pharmaceutics. 2020 Mar 1;12(3).

36. Counil C, Abenojar E, Perera R, Exner AA. Extrusion: A New Method for Rapid Formulation of High-Yield, Monodisperse Nanobubbles. Small. 2022 Jun 1;18(24).

37. Hernandez C, Gulati S, Fioravanti G, Stewart PL, Exner AA. Cryo-EM Visualization of Lipid and Polymer-Stabilized Perfluorocarbon Gas Nanobubbles - A Step Towards Nanobubble Mediated Drug Delivery. Sci Rep. 2017 Dec 1;7(1).

38. Abenojar EC, Nittayacharn P, De Leon AC, Perera R, Wang Y, Bederman I, et al. Effect of Bubble Concentration on the in Vitro and in Vivo Performance of Highly Stable Lipid Shell-Stabilized Micro- And Nanoscale Ultrasound Contrast Agents. Langmuir. 2019 Aug 6;35(31):10192–202.

39. Jafari Sojahrood A, de Leon AC, Lee R, Cooley M, Abenojar EC, Kolios MC, et al. Toward Precisely Controllable Acoustic Response of Shell-Stabilized Nanobubbles: High Yield and Narrow Dispersity. ACS Nano. 2021 Mar 23;15(3):4901–15.

40. Cooley MB, Abenojar EC, Wegierak D, sen Gupta A, Kolios MC, Exner AA. Characterization of the interaction of nanobubble ultrasound contrast agents with human blood components. Bioact Mater. 2023 Jan 1;19:642–52.

41. Jeon HJ, Qureshi MM, Lee SY, Badadhe JD, Cho H, Chung E. Laser speckle decorrelation time-based platelet function testing in microfluidic system. Sci Rep [Internet]. 2019;9(1):1–8. Available from: http://dx.doi.org/10.1038/s41598-019-52953-5

42. Wegierak D, Cooley M, Perera R, Wulftange WJ, Gurkan UA, Kolios MC, et al. Decorrelation Time Mapping as an Analysis Tool for Nanobubble-Based Contrast Enhanced Ultrasound Imaging. BioRxiv [Internet]. 2022; Available from: https://doi.org/10.1101/2022.12.21.521428

43. Chen YQ, Kuo JC, Wei MT, Wu MC, Yang MH, Chiou A. Fibroblast Promotes Head and Neck Squamous Cell Carcinoma Cell Invasion through Mechanical Barriers in 3D Collagen Microenvironments. ACS Appl Bio Mater. 2020 Sep 21;3(9):6419–29.

44. Munir MU. Nanomedicine Penetration to Tumor: Challenges, and Advanced Strategies to Tackle This Issue. Cancers (Basel). 2022 Jun 1;14(12).

45. Blanco E, Shen H, Ferrari M. Principles of nanoparticle design for overcoming biological barriers to drug delivery. Nat Biotechnol. 2015 Sep 8;33(9):941–51.

46. Guo P, Liu D, Subramanyam K, Wang B, Yang J, Huang J, et al. Nanoparticle elasticity directs tumor uptake. Nat Commun. 2018 Dec 1;9(1).

47. Cooley M, Sarode A, Hoore M, Fedosov DA, Mitragotri S, Sen Gupta A. Influence of particle size and shape on their margination and wall-adhesion: implications in drug

delivery vehicle design across nano-to-micro scale. Nanoscale. 2018 Aug 28;10(32):15350–64.

48. Kong SM, Costa DF, Jagielska A, van Vliet KJ, Hammond PT. Stiffness of targeted layer-by-layer nanoparticles impacts elimination half-life, tumor accumulation, and tumor penetration. Proceedings of the National Academy of Sciences. 2021;118(42).

49. Shi J, Kantoff PW, Wooster R, Farokhzad OC. Cancer nanomedicine: Progress, challenges and opportunities. Nat Rev Cancer. 2017 Jan 1;17(1):20–37.

50. Feiner-Gracia N, Glinkowska Mares A, Buzhor M, Rodriguez-Trujillo R, Samitier Marti J, Amir RJ, et al. Real-Time Ratiometric Imaging of Micelles Assembly State in a Microfluidic Cancer-on-a-Chip. ACS Appl Bio Mater. 2021 Jan 18;4(1):669–81.

51. Liu P, Zhang A, Zhou M, Xu Y, Xu LX. Real time 3D detection of nanoparticle liposomes extravasation using laser confocal microscopy. In: Annual International Conference of the IEEE Engineering in Medicine and Biology - Proceedings. 2004. p. 2662–5.

52. Hashizume H, Baluk P, Morikawa S, Mclean JW, Thurston G, Roberge S, et al. Openings between Defective Endothelial Cells Explain Tumor Vessel Leakiness. Am J Pathol. 2000;156:1363–80.

53. Hobbs SK, Monsky WL, Yuan F, Roberts WG, Griffith L, Torchilin VP, et al. Regulation of transport pathways in tumor vessels: Role of tumor type and microenvironment. Proceedings of the National Academy of Sciences. 1998 Apr 14;95(8):4607–12.

54. Willis AL, Sabeh F, Li XY, Weiss SJ. Extracellular matrix determinants and the regulation of cancer cell invasion stratagems. J Microsc. 2013 Sep;251(3):250–60.

55. van Dijk CGM, Brandt MM, Poulis N, Anten J, van der Moolen M, Kramer L, et al. A new microfluidic model that allows monitoring of complex vascular structures and cell interactions in a 3D biological matrix. Lab Chip. 2020;20(10):1827–44.

56. Oh BH, Kim KH, Chung KY. Skin Imaging Using Ultrasound Imaging, Optical Coherence Tomography, Confocal Microscopy, and Two-Photon Microscopy in Cutaneous Oncology. Front Med (Lausanne). 2019 Nov 22;6.

57. Gerdes MJ, Sood A, Sevinsky C, Pris AD, Zavodszky MI, Ginty F. Emerging understanding of multiscale tumor heterogeneity. Vol. 4, Frontiers in Oncology. Frontiers Media S.A.; 2014.

58. Malandrino A, Mak M, Kamm RD, Moeendarbary E. Complex mechanics of the heterogeneous extracellular matrix in cancer. Vol. 21, Extreme Mechanics Letters. Elsevier Ltd; 2018. p. 25–34.

59. Nagy JA, Chang SH, Shih SC, Dvorak AM, Dvorak HF. Heterogeneity of the tumor vasculature. Semin Thromb Hemost. 2010;36(3):321–31.

60. Viti J, Mori R, Guidi F, Versluis M, Jong N, Tortoli P. Correspondence-Nonlinear oscillations of deflating bubbles. IEEE Trans Ultrason Ferroelectr Freq Control. 2012;59(12):2818–24.

61. Dayton P, Klibanov A, Brandenburger G, Ferrara K. Acoustic radiation force in vivo: a mechanism to assist targeting of microbubbles. Ultrasound Med Biol. 1999 Oct;25(8):1195–201.

62. Acconcia CN, Leung BYC, Winch G, Wang J, Hynynen K, Goertz DE. Acoustic radiation force induced accumulation and dynamics of microbubbles on compliant surfaces. Phys Med Biol. 2019 Jul 2;64(13).

63. Afadzi M, Myhre OF, Yemane PT, Bjorkoy A, Torp SH, van Wamel A, et al. Effect of Acoustic Radiation Force on the Distribution of Nanoparticles in Solid Tumors. IEEE Trans Ultrason Ferroelectr Freq Control. 2021 Mar 1;68(3):432–45.

64. Rychak JJ, Klibanov AL, Hossack JA. Acoustic radiation force enhances targeted delivery of ultrasound contrast microbubbles: in vitro verification. IEEE Trans Ultrason Ferroelectr Freq Control. 2005 Mar;52(3):421–33.

65. Shah PN, Lin TY, Aanei IL, Klass SH, Smith BR, Shaqfeh ESG. Extravasation of Brownian Spheroidal Nanoparticles through Vascular Pores. Biophys J. 2018 Sep;115(6):1103–15.

66. Zhao H, Shaqfeh ESG, Narsimhan V. Shear-induced particle migration and margination in a cellular suspension. Physics of Fluids. 2012 Jan;24(1):011902.

67. Wiederhielm C, Black L. Osmotic interaction of plasma proteins with interstitial macromolecules. American Journal of Physiology-Legacy Content. 1976 Aug 1;231(2):638–41.

68. Aggarwal P, Hall JB, McLeland CB, Dobrovolskaia MA, McNeil SE. Nanoparticle interaction with plasma proteins as it relates to particle biodistribution, biocompatibility and therapeutic efficacy. Adv Drug Deliv Rev. 2009 Jun;61(6):428–37.

69. Saptarshi SR, Duschl A, Lopata AL. Interaction of nanoparticles with proteins: relation to bio-reactivity of the nanoparticle. J Nanobiotechnology. 2013 Dec 19;11(1):26.

70. Park SJ. Protein–Nanoparticle Interaction: Corona Formation and Conformational Changes in Proteins on Nanoparticles</p>. Int J Nanomedicine. 2020 Aug;Volume 15:5783–802.

71. Müller K, Fedosov DA, Gompper G. Margination of micro- and nano-particles in blood flow and its effect on drug delivery. Sci Rep. 2014 May 2;4.

72. He X, Yang Y, Han Y, Cao C, Zhang Z, Li L, et al. Extracellular matrix physical properties govern the diffusion of nanoparticles in tumor microenvironment. Proceedings of the National Academy of Sciences. 2023 Jan 3;120(1).

73. Chen JF, Fowlkes JB, Carson PL, Rubin JM, Adler RS. Autocorrelation of integrated power Doppler signals and its application. Ultrasound Med Biol. 1996;22(8):1057–70.

74. Carroll-Nellenback JJ, White RJ, Wood RW, Parker KJ. Liver Backscatter and the Hepatic Vasculature's Autocorrelation Function. Acoustics. 2020 Mar 1;2(1).

75. Hedrick WR, Hykes DL. Autocorrelation Detection in Color Doppler Imaging A Review. Journal of Diagnostic Medical Sonography. 1995;11:16–22.

76. Liu J, Levine AL, Mattoon JS, Yamaguchi M, Lee RJ, Pan X, et al. Nanoparticles as image enhancing agents for ultrasonography. Phys Med Biol. 2006 May 7;51(9):2179–89.

77. Chen F, Ma M, Wang J, Wang F, Chern SX, Zhao ER, et al. Exosome-like silica nanoparticles: a novel ultrasound contrast agent for stem cell imaging. Nanoscale. 2017;9(1):402–11.